Effect of sidewall on heat transfer and flow structure in Rayleigh–Bénard convection

Zhen-Hua Wan[1,2], Ping Wei[3], Roberto Verzicco[2,4,7], Detlef Lohse[2,5], Guenter Ahlers[6] and Richard J. A. M. Stevens[2],†

[1]Department of Modern Mechanics, University of Science and Technology of China, Hefei 230027, PR China

[2]Physics of Fluids Group, Max Planck Center Twente for Complex Fluid Dynamics, MESA+ Institute, and J. M. Burgers Center for Fluid Dynamics, University of Twente, 7500AE Enschede, The Netherlands

[3]School of Aerospace Engineering and Applied Mechanics, Tongji University, Shanghai, PR China

[4]Dipartimento di Ingegneria Industriale, University of Rome 'Tor Vergata', Via del Politecnico 1, Roma 00133, Italy

[5]Max Planck Institute for Dynamics and Self-Organization, Am Fassberg 17, 37077 Göttingen, Germany

[6]Department of Physics, University of California, Santa Barbara, CA 93106, USA

[7]Gran Sasso Science Institute, Viale F. Crispi 7, 67100 L'Aquila, Italy

In Rayleigh–Bénard convection experiments, the thermal coupling between the sidewall and fluid is unavoidable. As a result, the thermal properties of the sidewall can influence the flow structure that develops. To get a better understanding of the influence of the sidewall, we performed a one-to-one comparison between experiments and direct numerical simulations (DNS) in aspect ratio (diameter over height) $\Gamma = 1.00$ samples. We focus on the global heat transport, i.e. the Nusselt number Nu, and the local vertical temperature gradients near the horizontal mid-plane on the cylinder axis and close to the sidewall. The data cover the range $10^5 \lesssim Ra \lesssim 10^{10}$ where Ra is the Rayleigh number. The Nu number obtained from experimental measurements and DNS, in which we use an adiabatic sidewall, agree well. The experiments are performed with several gases, which have widely varying thermal conductivities, but all have a Prandtl number $Pr \approx 0.7$. For $Ra \gtrsim 10^7$, both experiments and DNS reveal a stabilizing (positive) temperature gradient at the cylinder axis. This phenomenon was known for high Pr, but had not been observed for small $Pr \approx 0.7$ before. The experiments reveal that the temperature gradient decreases with decreasing Ra and eventually becomes destabilizing (negative). The decrease appears at a higher Ra when the sidewall admittance, which measures how easily the heat transfers from the fluid to the wall, is smaller. However, the simulations with an adiabatic sidewall do not reproduce the destabilizing temperature gradient at the cylinder axis in the low Ra number regime. Instead, these simulations show that the temperature gradient increases with decreasing Ra. We find that the simulations can reproduce the experimental findings on the temperature gradient at the cylinder axis qualitatively when we consider the physical properties of the sidewall and the thermal shields. However, the temperature gradients obtained from experiments and simulations do

† Email address for correspondence: r.j.a.m.stevens@utwente.nl

not agree quantitatively. The reason is that it is incredibly complicated to reproduce all experimental details accurately due to which it is impossible to reproduce all experimental measurement details. The simulations show, in agreement with the models of Ahlers (*Phys. Rev.* E, vol. 63 (1), 2000, 015303) and Roche *et al.* (*Eur. Phys. J.* B, vol. 24 (3), 2001, pp. 405–408), that the sidewall can act as an extra heat conductor, which absorbs heat from the fluid near the bottom plate and releases it into the fluid near the top plate. The importance of this effect decreases with increasing *Ra*. A crucial finding of the simulations is that the thermal coupling between the sidewall and fluid can strongly influence the flow structure, which can result in significant changes in heat transport. Since this effect goes beyond a simple short circuit of the heat transfer through the sidewall, it is impossible to correct experimental measurements for this effect. Therefore, careful design of experimental set-ups is required to minimize the thermal interaction between the fluid and sidewall.

Key words: Bénard convection

1. Introduction

Rayleigh–Bénard convection, i.e. the convection of a horizontal fluid layer heated from below and cooled from above, is an excellent model system to study heat transfer and thermally induced turbulence. For reviews we refer the reader to, for example, Bodenschatz, Pesch & Ahlers (2000), Ahlers (2009), Ahlers, Grossmann & Lohse (2009), Lohse & Xia (2010), Chillà & Schumacher (2012) and Xia (2013). Thermally driven convection is relevant for atmospheric and oceanic flows as well as in numerous industrial processes. One of the important questions is how the heat transfer, which in dimensionless form is expressed as the Nusselt number $Nu = QL/(\lambda \Delta)$, depends on the Rayleigh number $Ra \equiv \beta g \Delta L^3/(\kappa \nu)$, the Prandtl number $Pr \equiv \nu/\kappa$ and the cell aspect ratio $\Gamma \equiv D/L$. Here D and L are the diameter and height of the convection cell, respectively, g is the gravitational acceleration, β is the isobaric thermal expansion coefficient, ν is the kinematic viscosity, κ is the thermal diffusivity and λ the thermal conductivity. The temperature difference between the plates is given by $\Delta \equiv T_h - T_c$, where T_h and T_c are the temperature of the bottom and top plate, respectively; Q is the heat flux per unit area crossing the fluid layer. Next to the heat transfer, also the time averaged temperature distribution and flow structure in this turbulent system are of great importance. Here we use new experimental measurements, which were performed using several compressed gases with $Pr \simeq 0.7$, and direct numerical simulations (DNS) for $Pr = 0.7$ in cylindrical samples with $\Gamma = 1.00$ to address both these issues.

For a fluid with a positive thermal expansion coefficient, the applied temperature difference in Rayleigh–Bénard convection is destabilizing in the Earth's gravitational field. Therefore, convection occurs when the temperature difference is large enough. It is well known that in high *Ra* number flow two thin thermal boundary layers, one below the top plate and one above the bottom plate, sustain most of the temperature difference (Ahlers *et al.* 2009). The sample interior, or bulk, is then at a nearly uniform temperature close to $T_M \equiv (T_h + T_c)/2$. Naively, one would expect that the temperature gradient in the bulk is destabilizing. Thus, it came as a surprise when measurements for *Ra* near 10^9 (Tilgner, Belmonte & Libchaber 1993; Brown & Ahlers 2007) and DNS for $Ra = 10^6$ (Schmalzl, Breuer & Hansen 2002; Breuer *et al.* 2004) showed that the temperature gradient in the bulk is stabilizing. The

measurements of time averaged local temperatures were for $Pr \simeq 5$ in the turbulent state. The DNS clearly showed a stabilizing vertical gradient of the horizontally averaged temperature for $Pr = 100$; but at that Pr and $Ra = 10^6$ the system, although probably time dependent, most likely was not turbulent (Krishnamurti 1970). For these high Pr number cases the thermal diffusivity κ is smaller than the kinematic viscosity ν. Therefore, one could argue that plumes emitted from the boundary layers have relatively long lifetimes and can travel along the sidewall to the opposite plate and then drift back to the sample centreline, which creates a stabilizing gradient in the sample interior. For lower Pr the plume lifetimes are expected to be shorter, and therefore one expects that it is more difficult for plumes to drift back to the sample centreline. However, surprisingly, we find that for $Ra \gtrsim 10^7$ and $Pr < 1$, when κ is larger than ν, the gradient at the sample centre remained stabilizing and of approximately the same size as found experimentally for $Pr \simeq 5$. However, in § 4.2 we show that the large scale circulation (LSC) velocity increases with decreasing Pr due to which plumes that are carried by the LSC can still cause a stabilizing temperature gradient at the cell centre for low Pr number fluids.

The influence of the sidewall on heat-transport measurements has been considered by several experimentalists, see, e.g. Ahlers (2000), Roche *et al.* (2001), Niemela & Sreenivasan (2003) and Ahlers *et al.* (2009). Rayleigh–Bénard containers are more complex (see, e.g. Niemela *et al.* (2000) and Zhong & Ahlers (2010)) than the idealized system with an adiabatic sidewall and isothermal top and bottom plates, which is usually considered in simulations. Experimental cells are limited by the physical properties of the available materials and working fluids. Thus effects like the finite conductivity of the sidewall and the configuration of the insulation and thermal shields might influence the heat transfer and flow structures. Often these effects are accounted for simply by subtracting the corresponding heat current transferred by an empty convection cell. The phenomenological models of Ahlers (2000) and Roche *et al.* (2001) already showed that the thermal coupling between fluid and sidewall makes this procedure in principle inadequate to account for the sidewall effect. The reason is that the vertical temperature profile in the sidewall differs from that in the convecting fluid and therefore there is a lateral heat exchange between sidewall and fluid, which can influence the flow dynamics. To further explore these issues, Verzicco (2002) performed DNS of Rayleigh–Bénard convection in a cylindrical container with $\Gamma = 1/2$ in which the effect of the finite conductivity of the sidewall was assessed. He found that for $Ra < 10^9$ the sidewall effect can change the exponent α of the power law $Nu \sim Ra^{\alpha}$ by up to 10%. Later simulations for the same geometry found that changes in the sidewall configurations can trigger different flow organizations (Stevens, Lohse & Verzicco 2014). To explore whether sidewall effects may be responsible for the stabilizing gradients seen in experiments, we performed experiments with various fluids and simulations with different sidewall configurations.

It is well known that the sidewall can have a strong influence on the critical Rayleigh number Ra_c for the onset of convection (Buell & Catton 1983; Hébert *et al.* 2010). In that case, Ra and thus also Ra_c for a given geometry are determined by the sidewall admittance, which measures how easily the heat transfers from the fluid to the wall,

$$C = \frac{D\lambda}{2d\lambda_w}. \tag{1.1}$$

Here λ is the thermal conductivity of the employed gas, and d and λ_w are the sidewall thickness and its thermal conductivity, respectively. For the ideal adiabatic case, $C = \infty$. Although it is not known whether C is the only important factor at high

Ra, we were particularly motivated by its influence near the onset. We investigate this by performing experimental measurements for $1 \lesssim C \lesssim 12$ by using different gases with nearly the same $Pr \simeq 0.7$, but different conductivities, to vary *C*. In addition to *Nu*, we determined the temperature gradients near the horizontal mid-plane both on the cylinder axis and close to the sidewall. While these gradients were stabilizing and (within our resolution) independent of the used fluid when *Ra* was high, they did depend on the chosen gas (and thus on *C*) for $Ra \lesssim 10^7$. For comparison, we performed simulations using the physical properties of neon with adiabatic boundary conditions at the side as well as with a wall domain with wall properties equal to those of the experiment included. While the adiabatic boundary condition corresponds to $C \rightarrow \infty$, see (1.1), the wall–neon combination has the same $C = 3.9$ as the experimental system. We also consider simulations with helium as working gas in a cell with a Plexiglas sidewall, which corresponds to $C = 12$, and additional insulation layers and sidewall shields.

The presented simulations are complementary to the experiments as the simulations allow us to study the flow structures in more detail. We also use the simulations to test various sidewall configurations to assess the influence of different sample designs. To achieve this we employ, in contrast to most DNS, a more realistic model based on the Navier–Stokes–Brinkman equation in combination with the immersed boundary method to simulate the effect of the sidewall and insulation layers as a conjugate heat transfer problem. A similar modelling approach was followed by Stevens *et al.* (2014). However, in contrast to the previous study, we now present a direct comparison between experiments and simulations. In addition, Stevens *et al.* (2014) mainly focused on the effect of the sidewall on the *Nu* number. However, now we also assess the effect of the thermal sidewall properties on the LSC. We will show that the sidewall can influence the LSC in such a way that a destabilizing temperature gradient at the cylinder axis is created for lower *Ra*. Clearly, this continuous effort to accurately model the interaction between the sidewall and flow dynamics using DNS is necessary to get a better understanding of the effect this interplay may have on the heat transfer and flow structures in Rayleigh–Bénard convection. However, we emphasize that due to the complicated interactions between fluid and sidewall, and the difficulty in identifying all relevant design parameters, it remains impossible to reproduce all experimental details.

The paper has the following structure: in §§ 2 and 3 we describe the experimental and numerical procedures. In § 4, we present the experimental measurements in comparison with the simulation results obtained with an ideal adiabatic sidewall. In an attempt to explain the differences between experiments and idealized simulations, we discuss the effect of the sidewall on the heat transport and flow dynamics in § 5. We conclude with a summary and conclusion in § 6.

2. The apparatus

The overall features of the apparatus were described in detail before by Zhong & Ahlers (2010). We used a sample with thick copper top and bottom plates and a Plexiglas (poly(methyl methacrylate)) sidewall of thickness $d_w = 6.4$ mm. The inside dimensions were $L = D = 190.5$ mm, yielding an aspect ratio $\Gamma = 1.00$.

A groove in the top and bottom plates directly below or above the sidewall contained an 'O'-ring that sealed the sidewall to the plates. Two aluminium brackets, one above the top and the other below the bottom plate, pressed the plates against the 'O'-rings and the sidewall. This compression was achieved by six steel tension

rods connecting the brackets and located at a diameter larger than that of the sidewall. A thin Teflon capillary penetrated the sidewall at mid-height and was used to fill the sample. Externally the capillary was connected to the fill line coming from the gas supply cylinder, as well as to a pressure gage (Paroscientific Model 745) and another volume known as the 'hot volume' (HV) (Mueller, Ahlers & Pobell 1976). The HV had a size similar to that of the sample, and its temperature could be adjusted in a feedback loop with the pressure gage to keep the sample pressure constant. Over several days the HV temperature typically increased because of the gradual diffusion of the sample gases through the Plexiglas sidewall of the sample. The diffusion rate is higher for the lighter gases. At a pressure of 4 bars, the HV heating rate was approximately 2×10^{-4} K s^{-1} when the sample was filled with helium and approximately 5×10^{-5} K s^{-1} when SF$_6$ was used. The acceptable temperature range for the HV was from $20\,^{\circ}$C to $60\,^{\circ}$C and this allowed operation for several days without adding more sample gas. We used sample pressures from 4 bars to somewhat below 1 bar.

The plate temperatures and the heat flux applied to a bottom-plate heater were used to determine the *Nu* number $Nu = \lambda_{eff}/\lambda$, where $\lambda_{eff} = LQ/\Delta$, and Q is the heat current. It is obtained as $Q = Q_t - Q_p$, where Q_t is the total current and Q_p the parasitic current, mainly through the sidewall. The total power Q_t dissipated in the bottom-plate heater was determined from the heater current and voltage. The parasitic current Q_p was based on measurement with a nearly empty cell where no convection took place. That measurement had to be corrected for the conductive heat current due to the remaining quiescent gas to yield Q_p. There were contributions to Q_p from several sources. Some of the currents passed through the foam insulation to an isothermal shield maintained at T_M. Another part was conducted by the tension rods to the water reservoir above the top plate. The sidewall conducted the remaining part. The current $Q = Q_t - Q_p$ was used to obtain a preliminary estimate Nu_0 of *Nu*. An estimate of the current Q_w passing through the sidewall based on the sidewall geometry and conductivity was then used to correct Nu_0 for the nonlinear sidewall effect, as discussed by Ahlers (2000) and Roche *et al.* (2001), to yield our final estimate of *Nu*.

While the above corrections to Q_t and Nu_0 typically are only of modest size when fluids such as water with relatively high conductivity are used, they become more critical for gases where the conductivities can be much smaller. For example, at $25\,^{\circ}$C the conductivities of water and SF$_6$ differ by a factor of approximately 50. For helium, the difference is approximately a factor 4. As we shall see below, there is good agreement between the *Nu* values obtained using all different working gases even though their conductivities vary significantly, see table 2, and the corrections to Q_t and Nu_0 differ widely.

There were six Honeywell type 111-104HAK-H01 thermistors inside the sample. Of these we used four in the present work. Their locations are given in table 1. Two each were mounted near the end of a ceramic rod (Omega ceramic thermocouple insulators of type FRA-005132) with an outside diameter of 0.90 mm as described elsewhere (Ahlers, Bodenschatz & He 2014; Wei & Ahlers 2014; He *et al.* 2015). Each thermistor lead passed through a 0.13 mm diameter hole in the rod and parallel to the rod axis. The rods were inserted through holes, also of nominally 0.90 mm diameter, in the 6.4 mm thick sidewall. The rods terminated near the outside of the sidewall, and there they as well as the uninsulated leads were sealed to the sidewall with epoxy. Four thermistors (held by two rods) were located on the sample axis. The remaining two were located near the sidewall at $\xi \equiv (D/2 - r)/(D/2) = 0.13$, where r is the horizontal distance from the cylinder axis. This means that $\xi = 1$ at the centre axis ($r = 0$) and $\xi = 0$ at the sidewall ($r = D/2$).

ID	$R - r$ (mm)	ξ	z (mm)	z/L	θ_{int}
V0-1	95	1.00	75.9	0.398	$15\pi/8$
V0-4	95	1.00	97.1	0.510	$7\pi/8$
V1-1	12	0.13	93.2	0.490	$\pi/8$
V1-2	12	0.13	97.2	0.510	$\pi/8$

TABLE 1. The identifiers, ID, and the radial and vertical locations of the internal thermistors. The sample height was $L = 190.5$ mm and the radius was $R = 95.2$ mm. The angle θ_{int} (in rad) is the azimuthal location (relative to an arbitrary origin) for each thermometer, measured in a counter-clockwise direction when viewed from above.

Sample	T (K)	Pr	$\beta/\kappa\nu$ (s^2 K^{-1} cm^{-4})	$10^3\lambda$ W cm^{-1} K^{-1}	C
SF_6	298	0.786	4.18	0.129	1.02
Nitrogen	298	0.724	0.0965	0.258	2.04
Neon	298	0.664	0.0144	0.496	3.91
Helium	298	0.675	0.00151	1.52	12.0

TABLE 2. Properties of the employed fluids at 25 °C and $P = 1$ bar. The Plexiglas sidewall conductivity was taken to be 0.0019 W cm^{-1} K^{-1}. The properties Pr, λ and C are nearly independent of the pressure P while $\beta/(\kappa\nu)$ is approximately proportional to P^2.

While the vertical hole locations in the sidewall were known with high accuracy, there were two possible contributions to the uncertainties of the vertical thermistor locations. One came from any tilt of the rods relative to a line orthogonal to the cylinder axis. We believe this to be very small, probably no more than 0.2 mm on the sample axis and much less near the sidewall. Another possible contribution came from the suspension of the thermistors by their 0.10 mm diameter platinum leads (see e.g. figure 2 of He *et al.* (2015)). Because of the fragile nature of these leads, there is an uncertainty of approximately 0.3 mm in the vertical position of the thermistor centre. Thus the total uncertainty is close to 0.5 mm. Similarly, we estimate that the uncertainty of the distance δz between the two thermistors used to measure the temperature gradient is approximately 0.7 mm.

We used the thermistor pairs (V0-1, V0-4) on the centreline ($\xi = 1.00$) and (V1-1, V1-2) near the sidewall ($\xi = 0.13$) for the temperature-gradient measurements, see table 1 for details. Thus for $\xi = 1.00$ the separation between the two sensors was $\delta z = 21.6 \pm 0.7$ mm, while for $\xi = 0.13$ it was only $\delta z = 4.0 \pm 0.7$ mm. The corresponding uncertainties of the gradients, due to the uncertainties of the measurement geometry, were $\pm 3\%$ for $\xi = 1.00$ and $\pm 17\%$ for $\xi = 0.13$.

We used the gases listed in table 2. Nearly all of the measurements were made with T_M close to 25 °C. Some of the sample properties at 25 °C and a pressure $P = 1$ bar are also given in the table. Each gas could be employed up to 4 bars. This allowed measurements over a little more than a decade of Ra for a given gas since Ra for gases is approximately proportional to P^2. The Ra-range covered was different for each gas because the parameter combination $\beta/\kappa\nu$ is different, see table 2.

In this work, we neglected the influence of the adiabatic temperature gradient, which can play a significant role in convection experiments using compressed gases (Landau & Lifshitz 1987; Chavanne *et al.* 1996; Ashkenazi & Steinberg 1999), especially near

their critical points. This gradient is given by

$$\frac{\Delta_{ad}}{\Delta} = \frac{\beta T_M g L}{C_p \Delta}, \tag{2.1}$$

where T_M is the absolute mean temperature and C_p is the heat capacity per unit mass. This gradient is largest for the heaviest gas; in our case for SF_6. However, even for SF_6, the adiabatic temperature gradient was well below 10^{-3}. Thus we did not make any corrections for this effect.

For our experiments, the shift $(T_0 - T_M)/\Delta$ of the centre temperature T_0 relative to the mean temperature of T_M spanned the range from 0.008 to 0.018. While this corresponds to samples that are usually regarded as being well represented by the Boussinesq approximation, these values are comparable to those that we report for the temperature gradients. However, in our view, the two are unrelated. While non-Oberbeck–Boussinesq (NOB) effects create unequal temperature drops across the two horizontal boundary layers, they leave the temperature variation (and thus the variations of any fluid properties) in the bulk quite small. Thus we think the modest NOB effects do not affect the results on the temperature gradient in the bulk.

For most of the explored Ra number range in this work the LSC consists of a single convection roll. In a perfect sample, where the only perturbation of the azimuthally invariant geometry is the Coriolis force due to Earth's rotation, one expects the LSC orientation to have a broad distribution with a maximum slightly north of west (see, e.g. Brown & Ahlers (2006, 2008*b*) and references therein). In a real sample, the azimuthal invariance often is also broken by unintended inhomogeneities, and the LSC circulation plane assumes a preferred orientation (Brown & Ahlers 2008*a*). In our case, the insertion of the ceramic rods carrying the thermistors breaks this invariance. Separate measurements using thermometers located in the sidewall at the horizontal mid-plane of the sample and at eight azimuthal positions (Brown, Nikolaenko & Ahlers 2005) showed that the downflow of the LSC had a preferred orientation near $\theta_d = 0.3$, i.e. very close to the location of the sensor position at $\theta_{int} = \pi/8$, see table 1. We would expect the downflow to be relatively cold, leading to a reduced mean temperature. It is not clear whether the downflow influenced the temperature gradient. As we only have one azimuthal measurement location, it is not possible to determine any statistical (or systematic) uncertainties in the measured mean temperature gradient. We expect that the preferred LSC orientation does not influence the temperature-gradient measurements at the sample centre.

3. Numerical procedures

In the simulations, we solve the non-dimensional Navier–Stokes equations within the Boussinesq approximation (Verzicco 2002; Stevens *et al.* 2014) in combination with an immersed boundary method (Fadlun *et al.* 2000) to account for the heat transfer in the sidewall and insulation layer. The corresponding equations read,

$$\frac{D\boldsymbol{u}}{Dt} = -\nabla p + \sqrt{\frac{Pr}{Ra}}\nabla^2 \boldsymbol{u} + \theta\hat{z} + \boldsymbol{f}, \quad \nabla \cdot \boldsymbol{u} = 0, \tag{3.1}$$

$$\frac{D\theta}{Dt} = \frac{1}{\sqrt{PrRa}}\frac{\rho_f C_f^p}{\rho C^p}\nabla \cdot \left(\frac{\lambda}{\lambda_f}\nabla\theta\right) + h, \tag{3.2}$$

where $\boldsymbol{f}$ and h are forcing terms whose values depend on the particular locations in the computational domain:

(i) $\boldsymbol{f} = 0$ and $h = 0$ in the fluid domain. The (3.1)–(3.2) reduce to the Navier–Stokes and convection–diffusion temperature equations.
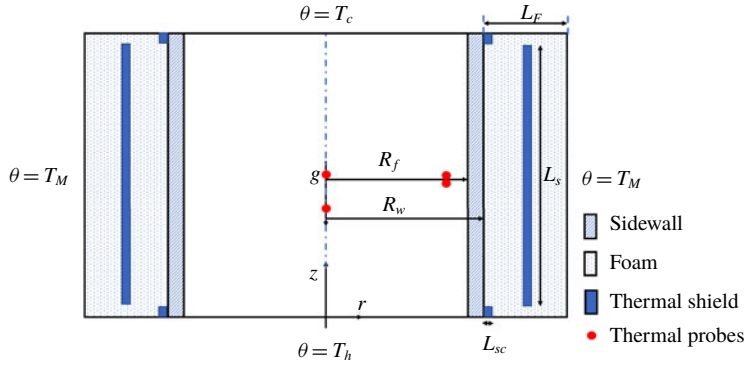
FIGURE 1. (Colour online) Sketch of numerical set-up with sidewall, insulation layer and thermal side shields. The aspect ratio of the fluid domain $\Gamma = 2R_f/L = 1$. The Plexiglas sidewall has a thickness $e = R_w - R_f = L/30$ such that $R_w = 0.53333L$. The insulation layer has a thickness $L_F = 0.2L$. For the inner thermal side shields $L_{sc} = 0.015L$ with square cross-section. The outer thermal shield has a thickness of $0.02L$ and a height $L_s = 0.96L$, and its inner edge is located at $0.6L$ from the cylinder axis. The outer surface of insulation layer is assumed to be isothermal at $\theta = (T_c + T_h)/2 = T_M$. The temperatures of the entire bottom and top plates are fixed at T_h and T_c, respectively. The thermal probes are placed at $z = 0.4L$ and $z = 0.51L$ for $\xi = 1.0$ ($r = 0$), while they are placed at $z = 0.49L$ and $z = 0.51L$ for $\xi = 0.13$ ($r = 0.435L$).

(ii) f is determined according to Fadlun *et al.* (2000) to ensure that $u = 0$ within the solid parts, i.e. sidewall and thermal shields, see figure 1. Similarly, h is computed to impose the desired temperature within the thermal shields while it is set to zero within those solid regions where temperature is to be determined as part of the solution.

(iii) $f = -u/K$ in the insulation layer, where K is the porosity. Equation (3.1) is then referred to as the Navier–Stokes–Brinkman equation. Here we use the same value as Stevens *et al.* (2014), i.e. $K = 10$, to ensure that the velocities in the insulation layer are an order of magnitude smaller than in the fluid. Within the insulation layer we set $h = 0$ since no conditions on the temperature are imposed.

In the above equations, θ is the non-dimensional temperature, u the velocity, p the pressure, $\hat{z}$ the unit vector pointing in the opposite direction to gravity. No-slip boundary conditions are employed at all solid surfaces and a constant temperature of T_h and T_c is used at the bottom and top plate, respectively. The equations are non-dimensionalized by the fluid sample height L, the temperature difference $\Delta = T_h - T_c$ between the plates, and the free-fall velocity $U = \sqrt{\beta g \Delta L}$. ρ, C^p and λ are, respectively, the density, the constant pressure specific heat and the thermal conductivity. The subscript f refers to the properties of the fluid, while the same quantities have different values in the sidewall or the insulation layer; R_f is the radius of the fluid domain and R_w the radius, including the sidewall thickness. The radial dimension of the computational domain is $R_w + L_f$, which also includes the insulating foam layer and the thermal shields when present. This allows the entire domain to be considered in a unified computational framework. Details about the implementation of the above scheme can be found in appendix A.

In §4, we compare the experimental measurements with simulations in which we use an ideal adiabatic sidewall. Subsequently, in §5, we consider the conjugate

heat transfer problem of a finite-thickness sidewall with physical properties. Initially, we only include the Plexiglas sidewall, assuming that the temperature boundary condition on the 'dry' side ($r = R_w$) is isothermal at $T_M = (T_c + T_h)/2$ to mimic the nearly constant environmental temperature provided by the insulation layer in the experimental apparatus (Zhong & Ahlers 2010). We note that no temperature boundary condition is required at the fluid–sidewall interface ($r = R_f$) since the temperature is solved within the entire computational domain. The bottom and top plates are assumed to extend until the edge of the sidewall, although it should be noted that this condition is strongly dependent on the method that is used to assemble the horizontal plates and the sidewall.

Finally, we simulate the whole set-up sketched in figure 1, in which we also include the insulation layer and the thermal side shields. The outer surface of the insulation layer is assumed to be isothermal at $\theta = (T_c + T_h)/2 = T_M$. The temperatures of the entire bottom and top plates are fixed at T_h and T_c, respectively. This set-up resembles the configuration considered by Stevens *et al.* (2014), but the geometrical parameters and physical properties are different and taken from the reference experiment described in the previous section. The specific geometrical parameters are given in figure 1, and the material properties are listed in table 2. When compared to the case with just the Plexiglas sidewall, this situation is much closer to the experimental apparatus, although we emphasize that the actual set-up is still more complex than presented in these simulations.

Details about the simulations, the documented *Nu* number data and the used resolution can be found in appendices B and C. In short, we consider three different configurations, (i) a standard Rayleigh–Bénard cell with an adiabatic sidewall, (ii) a Rayleigh–Bénard cell using neon ($Pr = 0.7$) as working fluid and just a Plexiglas sidewall and (iii) a cell with a Plexiglas sidewall, additional insulation layer and thermal side shields as indicated in figure 1 filled with neon and helium, respectively. All simulations are performed for $\Gamma = 1.00$.

The code has been used before by Stevens *et al.* (2014), where validations against different simulation (Shishkina & Thess 2009; Hébert *et al.* 2010; Scheel, Kim & White 2012) and experimental results were provided. For all the simulations, the *Nu* number is computed by determining the heat flux crossing the fluid through the plates $Q_f = \int_0^{2\pi} \int_0^{R_f} \lambda_f \boldsymbol{\nabla}\theta \mid_{z=0} \cdot \boldsymbol{n} \, \mathrm{d}S/(\pi R_f^2)$. This is slightly different from what is done in the experiments where the total heat flux that enters through the hot plate is measured ($Q_T = \int_0^{2\pi} \int_0^{R_T} \lambda_f \boldsymbol{\nabla}\theta \mid_{z=0} \cdot \boldsymbol{n} \, \mathrm{d}S/(\pi R_T^2)$), which only afterwards is corrected for the parasitic heat current flowing through the sidewall. It is worth noticing that the latter is determined by empirical models. Therefore the uncertainty in this correction might be responsible for some of the later encountered discrepancies between the *Nu* numbers obtained from experiments and simulations. At the end of § 5, we discuss other potential reasons for discrepancies.

In the simulations, we calculate the temperature gradients using flow data obtained from the probe locations used in the experiments, see table 1. Even though we performed the simulations for a very long time, up to 10 000 free-fall time units for lower *Ra* and for approximately 300 time units for the highest *Ra*, the statistical convergence of the simulation data is still not as good as for the experimental data. To improve the convergence of the simulation data, we calculate the azimuthally averaged temperature gradient close to the sidewall ($\xi = 0.13$). At the cylinder axis ($\xi = 1.00$) we use the top–down symmetry in the simulations and report the average temperature gradient obtained from two measurements, i.e. ones between $z/L = 0.40$ and $z/L = 0.51$ and ones between $z/L = 0.49$ and $z/L = 0.60$. Because, we cannot
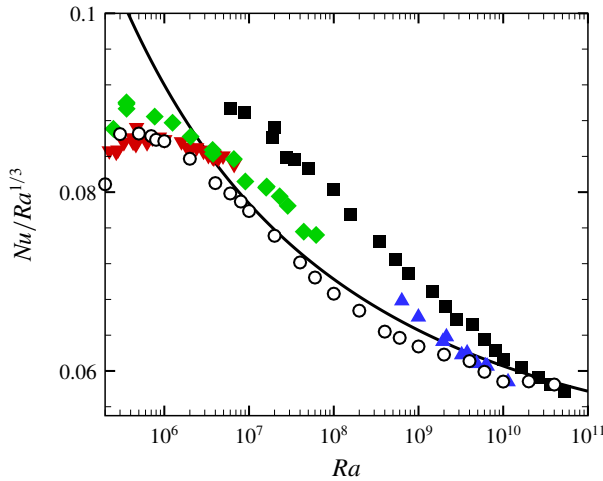
FIGURE 2. (Colour online) Value of $Nu/Ra^{1/3}$ as a function of Ra for $\Gamma = 1.00$ and $Pr \simeq 0.7$. Solid line: prediction of the unifying theory (Grossmann & Lohse 2000; Stevens *et al.* 2013) for $Pr = 0.7$. Open circles: DNS with an adiabatic sidewall for $Pr = 0.7$. Solid symbols: experimental data of Niemela & Sreenivasan (2003) using helium at temperatures near 5.3 K with Pr in the range from 0.68 to 0.71 (black square), new experimental results using helium ($Pr = 0.68$, red down-pointing triangles), neon ($Pr = 0.66$, green diamonds) and SF_6 ($Pr = 0.79$, blue up-pointing triangles).

perform an azimuthal average at the cylinder axis the statistical uncertainty for the temperature gradient is higher at the cylinder axis than close to the sidewall, especially for $Ra \geqslant 6 \times 10^8$ when the simulation length is more limited.

4. Measurements compared to simulations with adiabatic sidewall

4.1. *Results for the Nu number*

Figure 2 shows a comparison of the compensated *Nu* versus *Ra* data obtained from our new measurements, and the simulations in which an adiabatic sidewall is used. The simulation results agree excellently with the predictions from the unifying theory for $Ra \gtrsim 2 \times 10^6$. However, for $Ra \lesssim 2 \times 10^6$, the simulations give a lower heat transfer than the unifying theory, because the flow is no longer turbulent, and the unifying theory does not apply to this regime. For comparison, figure 2 also shows, as solid black squares, the experimental *Nu* results of Niemela & Sreenivasan (2003). While these data agree with the DNS for $Ra \gtrsim 10^{10}$, they are larger than the simulation results for lower *Ra*, with the difference reaching 16 % below $Ra \simeq 10^9$. The experimental measurements presented here agree very well with the DNS for $Ra \gtrsim 10^9$. As *Ra* decreases below 10^9, they gradually rise above the simulation results, although the difference never exceeds 6 %. Interestingly, the measurement data also agree very well with the simulation results for $Ra \lesssim 2 \times 10^6$ and show the same maximum of the compensated *Nu* number near $Ra = 10^6$. It thus seems that the influence of the sidewall on the measured *Nu* number is limited when appropriate corrections are applied to the measurements.

4.2. *Results for the temperature gradients*

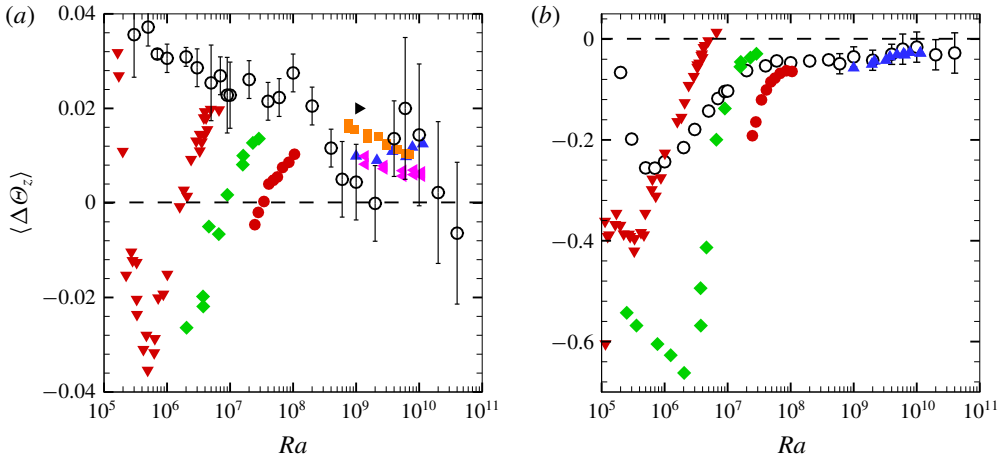In figure 3 we report results for the dimensionless vertical temperature gradient

FIGURE 3. (Colour online) The mean vertical temperature gradient (*a*) on the cylinder axis ($\xi = 1.00$) and (*b*) close to the sidewall ($\xi = 0.13$). Please note the different scales of the two vertical axes. Open circles: DNS results using an adiabatic sidewall. Solid symbols: new experimental results using helium (red down-pointing triangles), neon (green diamonds), nitrogen (red circles) and SF_6 (blue up-pointing triangles). Solid orange squares and pink left-pointing triangles: experimental results from Brown & Ahlers (2007) for $Pr = 4.4$ and $Pr = 5.5$, respectively. Solid black right-pointing triangles: result of Tilgner *et al.* (1993) for $Pr = 6.6$.

$$\langle \Delta \Theta_z(\xi) \rangle = \frac{\langle T(\xi, z_2) \rangle - \langle T(\xi, z_1) \rangle}{z_2 - z_1} \frac{L}{(T_h - T_c)}, \qquad (4.1)$$

where z_1 and z_2, $z_2 > z_1$, are positions along a vertical (z) axis pointing in a direction opposite to gravity. Here $\langle \cdots \rangle$ indicates the time average. Note that in absence of convection (when the temperature gradient is independent of z) $\langle \Delta \Theta_z \rangle = -1$. A positive value indicates a temperature profile that is stabilizing in the presence of gravity.

Figure 3(*a*) shows results for $\xi = 1.00$, i.e. along the sample axis. One sees that the experimental results using SF_6 (solid blue up-pointing triangles, $Pr = 0.786$) correspond approximately to $\langle \Delta \Theta_z \rangle = +0.01$, a small but definitely stabilizing gradient. This result is only somewhat smaller than the earlier measurement by Tilgner *et al.* (1993) for $Pr = 6.6$ (solid black right-pointing triangle) and of about the same size as the data by Brown & Ahlers (2007) for $Pr = 4.4$ and $Pr = 5.5$ (solid orange squares and pink left-pointing triangles). Our DNS results for $Pr = 0.7$ are shown as black open circles; they also reveal a small stabilizing gradient and some wiggling in the high Ra regime. The latter is presumably due to the uncertainty in the temperature gradient measured at the cylinder axis in the simulations, for a more detailed discussion see the end of § 3; clearly, the wiggling does not seem to be statistically relevant.

For higher Pr it was argued that the stabilizing temperature gradient emerges due to the relatively long lifetime of the plumes which allows them to travel along the sidewall to the opposite plate and then drift back to the sample centreline, which creates a stabilizing gradient in the sample interior (Tilgner *et al.* 1993; Brown & Ahlers 2007). To get a better understanding of this phenomenon, we estimate the plume lifetime $\tau_p = \lambda_\theta^2/\kappa$, where λ_θ is the thermal boundary layer thickness, and the

LSC travel time from the bottom to top conducting plates $\tau_{LSC} = L/U$, with U the velocity of the LSC, from which we obtain that

$$\frac{\tau_p}{\tau_{LSC}} = \frac{PrRe}{4Nu^2},\qquad(4.2)$$

where $Re = UL/\nu$ is the Reynolds number of the LSC. Our experiments and simulations are in regime IV_u of the unifying theory (Grossmann & Lohse 2001). To estimate the scaling of τ_p/τ_{LSC} with Ra and Pr we use, for simplicity, that $Nu \sim Ra^{1/3}$ and the result from the unifying theory that $Re \sim Pr^{-2/3}Ra^{4/9}$ in regime IV_u. This implies that $\tau_p/\tau_{LSC} \sim Ra^{-2/9}Pr^{1/3}$, which means that the Pr dependence of τ_p/τ_{LSC} is much weaker than one would naively expect. This shows that with decreasing Pr, the increased LSC speed allows the transported plumes to still create a stabilizing temperature gradient at the cell centre with a similar magnitude as in high Pr number fluids. We also note that the decrease of τ_p/τ_{LSC} with increasing Ra is in agreement with the observed reduction and eventual disappearance of the stabilizing mean temperature gradient at the cell centre.

As Ra is decreased, there are experimental data taken with nitrogen (solid red circles), neon (solid green diamonds) and helium (solid red down-pointing triangles) as working fluid. Each fluid covers a different range of Ra, always showing a stabilizing gradient at the higher Ra of the scanned range. As Ra decreases, the temperature gradient becomes more destabilizing. Surprisingly, the Ra value of the zero crossings depends on the fluid. Since all fluids have about the same Pr, the quantitative difference must be related to a different relationship between the thermal properties of the fluid and the sidewall. To a large extent, this can be captured by the value of the sidewall admittance C, see (1.1). While C is the only relevant parameter that determines the critical Rayleigh number Ra_c, it is not clear that C alone determines the system behaviour in the turbulent state. However, we note that the zero crossing of the gradient decreases monotonically with increasing C, see table 2 for values of C. This suggests that for the adiabatic case ($C \to \infty$) the decrease in $\langle\Delta\theta_z\rangle$ with decreasing Ra vanishes, just as in the adiabatic DNS.

As Ra is reduced even further, the helium data indicate a sharp transition at $Ra \simeq 4 \times 10^5$. For the other gases, the data do not extend to sufficiently small Ra to pass through a transition. We note that the Ra value of the transition is consistent with the onset of turbulence as reported by Heslot, Castaing & Libchaber (1987).

Returning to the DNS data for the system with adiabatic walls (open circles in figure 3a), we see that they behave quite differently as Ra decreases. They remain stabilizing down to the smallest Ra investigated ($Ra \simeq 3 \times 10^5$), with the magnitude of the gradient increasing as Ra decreases. Again, this is not inconsistent with the experimental data when we consider that an adiabatic sidewall may be considered as the limit $C \to \infty$. As Ra is further reduced, the temperature gradient in the simulations becomes negative (unstable stratification) for $Ra \approx 10^4$, while it becomes -1 at the onset, just as expected.

Figure 3(b) shows the gradient near the sidewall for $\xi = 0.13$. Here the gradient is destabilizing also for $Ra \gtrsim 10^8$ but of quite a small magnitude. In this range, the experimental data agree well with the adiabatic DNS results. The magnitude of the gradient increases, i.e. the gradient decreases, quite rapidly when Ra decreases. Again the Ra value where this rapid decrease begins depends on the used gas. Also here we see a sharp transition as Ra is decreased further, for helium at $Ra \simeq 3 \times 10^5$ and for neon at $Ra \simeq 2 \times 10^6$. While all gases yield qualitatively similar behaviour,
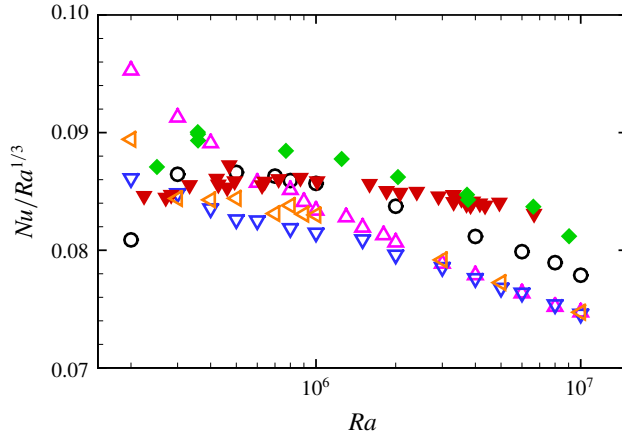
FIGURE 4. (Colour online) Comparison of the heat transport obtained in simulations using an adiabatic sidewall (open black circles), using a Plexiglas sidewall with neon as working fluid (open pink up-pointing triangles), using the Plexiglas sidewall with working fluid neon with additional insulation layer and thermal side shields (open blue down-pointing triangles) and using the Plexiglas sidewall with working fluid helium with additional insulation layer and thermal side shields (open orange left-pointing triangles). New experimental results using helium ($Pr = 0.68$, solid red down-pointing triangles) and neon ($Pr = 0.66$, solid green diamonds).

the quantitative difference again is presumably due to the difference in the sidewall admittance, see table 2.

We observe that the Navier–Stokes equations with the Boussinesq approximation, once made non-dimensional, depend only on Ra, Pr, and through the boundary conditions on Γ. The dependence of the temperature gradients on the specific fluid properties suggests that other physical effects play a role. The main effect is the conjugate heat transfer between the fluid and the sidewall system. As discussed above, it is not clear whether the sidewall admittance C can entirely characterize this phenomenon. To better understand this influence, we will discuss the effect of the sidewall and its influence on heat transport and flow structures as observed in simulations in the next section.

5. Effect of the sidewall

Figure 4 compares the heat transport obtained in simulations using the properties of neon and helium as working fluid and those of Plexiglas for the sidewall, with and without the additional insulation layer and thermal side shields as sketched in figure 1. The reference results for an adiabatic sidewall are also reported. Figure 4 shows that for $Ra \gtrsim 8 \times 10^5$ the heat transport is slightly smaller than the reference case when the Plexiglas sidewall is considered and at $Ra = 10^7$ the difference is approximately 4 %. However, for $Ra \lesssim 5 \times 10^5$ the heat transport in the cell with the Plexiglas sidewall is higher than in the reference cell and at $Ra = 2 \times 10^5$ this difference grows to approximately 15 %. When the insulation layer and thermal shields are added, their effects become significant only for $Ra \leqslant 2 \times 10^6$ with lower heat transport.

To explain this influence, we analyse the heat flux through the sidewall (Verzicco 2002). Figure 5 shows the lateral local Nu number $Nu_l(z) = \langle -\partial_r\theta \rangle_{t,\phi}(z)$ where ∂_r denotes the partial derivative with respect to r, at the interface of the fluid (neon)
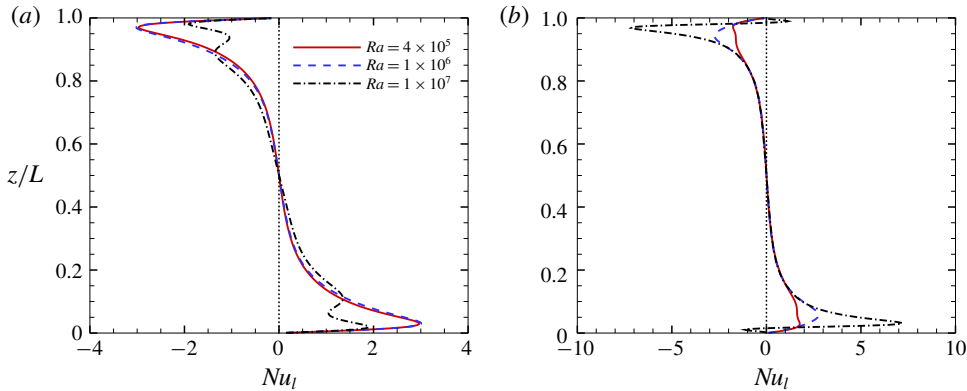
FIGURE 5. (Colour online) Time and azimuthally averaged heat transfer through the sidewall for (*a*) the simulations with neon with just the Plexiglas sidewall and (*b*) the simulations with the Plexiglas sidewall, the additional insulation layer and thermal side shields.

and the Plexiglas sidewall, and ϕ is the corresponding azimuthal angle over which we average. This gradient is determined by extrapolating the results from the fluid and sidewall domain separately while taking into account the conductivity ratio and then match them at the exact location ($r = R_f$) of the sidewall,

$$Nu_l = \frac{Q_w}{\lambda_f \Delta / L} = \left. \frac{\mathrm{d}T}{\mathrm{d}r} \right|_{r \to R_f^-} = \left. \frac{\lambda_s}{\lambda_f} \frac{\mathrm{d}T}{\mathrm{d}r} \right|_{r \to R_f^+}, \qquad (5.1)$$

where R_f^- and R_f^+ indicate that the temperature gradient at the sidewall is determined from the fluid and sidewall side, respectively. The largest heat flux through the sidewall is measured near the junction between the sidewall and horizontal plates. The profile reveals that the sidewall acts as an extra heat conductor, which absorbs part of the heat from the fluid near the bottom plate and releases it into the fluid near the top plate, thus acting as a short circuit. The relative importance of the short circuit is higher for lower Ra. For all cases, the vertically integrated heat flux through the entire sidewall is zero. Figure 5 shows that the lateral heat flux is skew–symmetric about the mid-plane. This means that the effect of the sidewall on the Nu number is not due to the main parasitic heat flux. Instead, the interaction between the sidewall and fluid causes a change in the flow structure, which changes the heat transfer that is supported by the flow. Figure 5 also reveals that for increasing Ra the heat flux through the sidewall near the plate can be higher when the additional insulation layer and thermal shields are added. The reason for this is the convection in the insulation layer, which we discuss below.

Figure 6 shows the local heat transfer, i.e. $Nu_{lb}(r) = \langle -\partial_z \theta \rangle_{t,\phi}(r)$, as a function of the radial position at the bottom plate for the different sidewall configurations using neon as working gas. The simulations with the adiabatic sidewall show a pronounced imprint of the LSC, due to which the local heat transport is highest at $r/L \sim 0.3$–0.4. When approaching the sidewall, the temperature gradient at the plate, and therefore the local heat transport, decrease. The pronounced imprint of the LSC decreases with increasing Ra, while the position of the maximum local heat transport shifts towards the sidewall. When the Plexiglas sidewall is added, the local heat
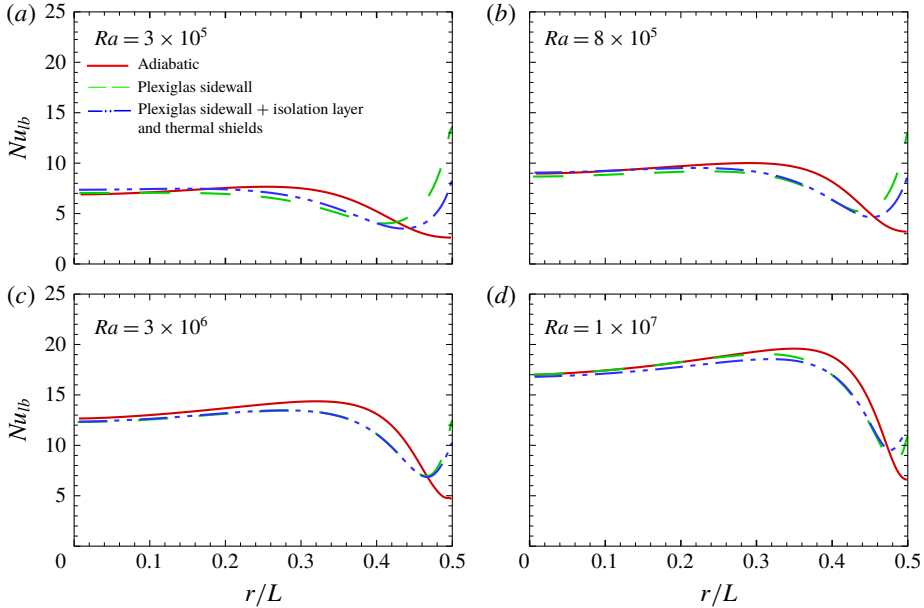
FIGURE 6. (Colour online) Time and azimuthally averaged local Nu_{lb} number at the plate as function of radial position for different Ra and different sidewall configurations with the working fluid neon.

transport is significantly increased close to the sidewall, especially at low Ra, due to the heat exchange between the sidewall and the fluid in the junction region. The local enhancement of the heat transport close to the sidewall, which is driven by the heat flux that passes through the sidewall, explains the higher overall Nu at low Ra when compared to the adiabatic case. Figure 6 clearly shows that for increasing Ra the heat transfer through the liquid overcomes all the secondary effects and the local heat-transport distribution converges for the different sidewall configurations as confirmed by the agreement of the heat transport in the high end of Ra observed in figure 4.

Figure 7 shows the time and azimuthally averaged root mean square (r.m.s.) temperature fluctuations, i.e. $\sqrt{\langle\theta'\rangle_{\phi,t}}$, for $Ra = 3 \times 10^5$, 10^6 and 10^7 for the three different model set-ups. When only an adiabatic sidewall is considered, the temperature fluctuations near the sidewall are the highest since the sidewall does not directly affect the temperature. The fluctuations are instead strongly damped when the Plexiglas sidewall is added; the reduction of the temperature fluctuations is caused by the relatively high heat capacity and steady temperature of the sidewall, induced by the isothermal condition imposed on the 'dry' side. This damping effect is absent with an ideal adiabatic sidewall, which is why the sidewall temperature is allowed to fluctuate freely. For the set-up with the additional insulation and thermal shield, we observe that there is almost no convection within the insulation layer at $Ra = 3 \times 10^5$ and 10^6. However, at $Ra = 10^7$ the thermal forcing strengthens and the convection in the porous material intensifies. This enhances the relative heat flux through the sidewall at $Ra = 10^7$, as shown in figure 5.

If we use the traditional definition of Ra number, and neglect the influence of the porosity, the Ra number inside the foam can be estimated. When neon ($\beta/k\nu = 0.0144$ (s^2 K^{-1} cm^{-4})) is used as working fluid, and we assume that the working fluid in the
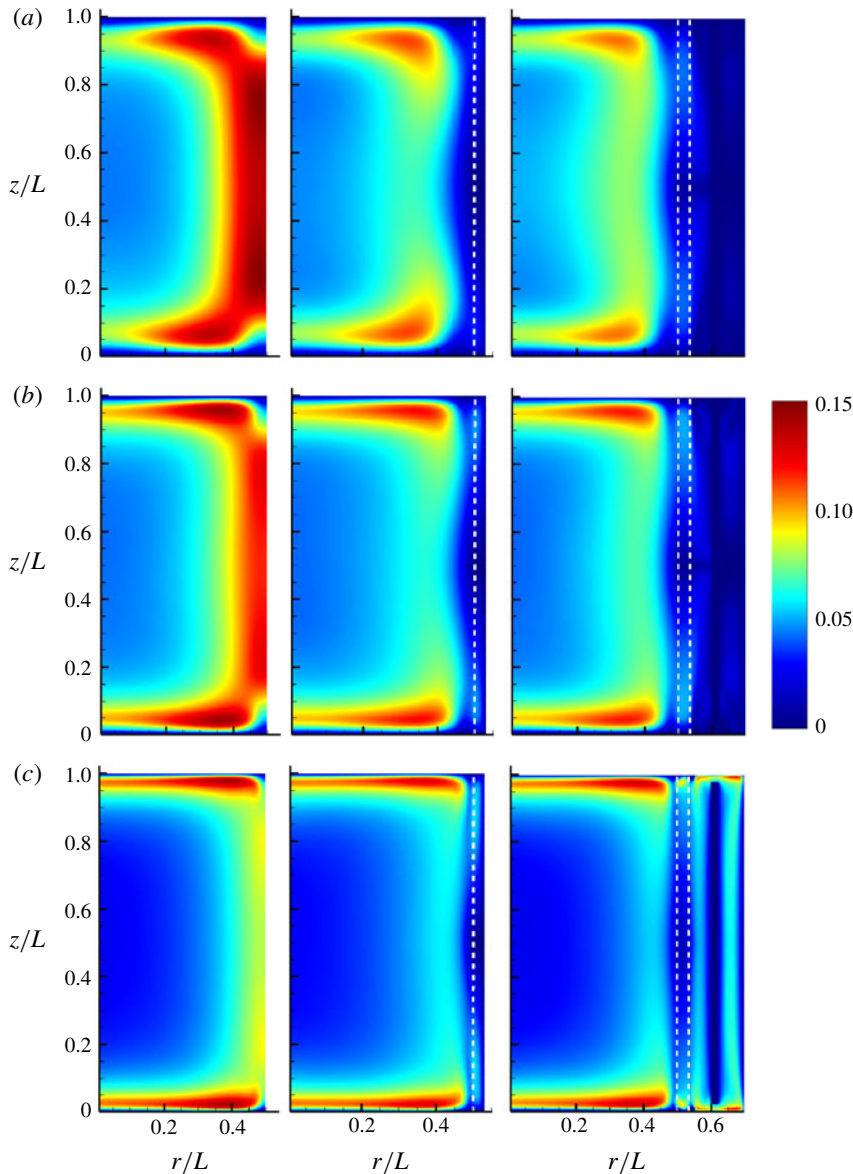
FIGURE 7. (Colour online) Azimuthally and time averaged r.m.s. temperature fluctuations for (*a*) $Ra = 3 \times 10^5$, (*b*) $Ra = 10^6$ and (*c*) $Ra = 10^7$ using neon as working fluid. The left, middle and right panels indicate the results for the adiabatic sidewall, Plexiglas sidewall and Plexiglas sidewall with additional insulation layer and thermal shields.

foam is air ($\beta/k\nu = 0.1034$ (s^2 K^{-1} cm^{-4})) and that the height and the temperature difference in the foam are identical to the fluid inside the cavity, this gives that for $Ra = 10^7$ the *Ra* number in the insulation layer is approximately $Ra \approx 7.2 \times 10^7$. However, we should emphasize that the complete set-up of the calculation is very complex and to define an appropriate *Ra* in the insulation layer is complicated.

Figure 8(*a*) shows that, in agreement with the experimental results, the temperature gradient at the cylinder axis ($\xi = 1.0$) becomes destabilizing in the low *Ra* number
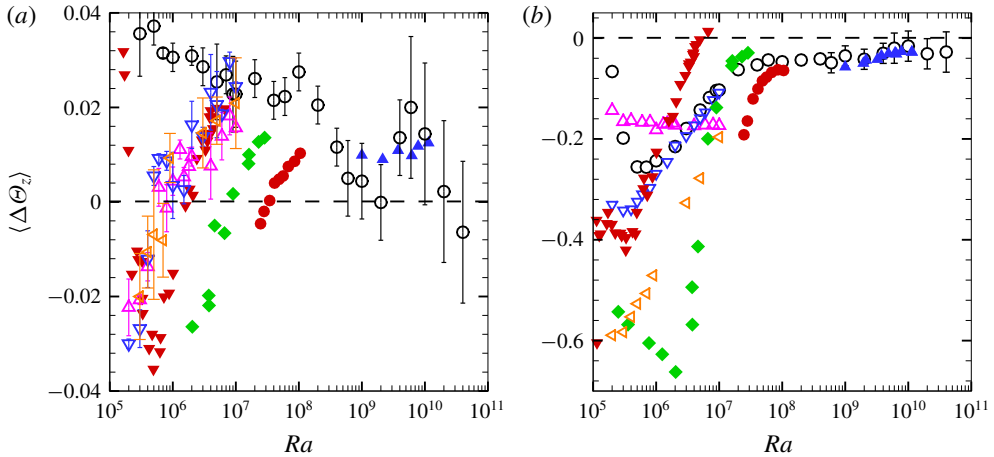
FIGURE 8. (Colour online) The mean temperature gradient (*a*) at the cylinder axis ($\xi = 1.00$) and (*b*) close to the sidewall ($\xi = 0.13$). Solid symbols: new experimental results using helium (red down-pointing triangles), neon (green diamonds), nitrogen (red circles) and SF_6 (blue up-pointing triangles). Open symbols: simulation results using an adiabatic sidewall (open circles), using a Plexiglas sidewall with neon as working fluid (pink open up-pointing triangles) and considering the Plexiglas sidewall with an additional insulation layer and thermal side shields (blue open down-pointing triangles), the Plexiglas sidewall with helium as working fluid with an additional insulation layer and thermal side shields (orange open left-pointing triangles).

regime when the Plexiglas sidewall is added. In the centre of the cell the effect of adding the additional insulation layer and thermal side shields is hardly visible. In addition, the results are also nearly identical for the two different working fluids, namely helium and neon, we consider in the simulations. This means that the simulations do not capture the trend of the temperature gradient with *C* that is observed in the simulations. However, we emphasize that a real laboratory set-up has much elements than just a physical sidewall, an isolation layer of foam, and thermal side shields. It is evident that the temperature gradient at the cylinder axis depends on modelling choices such as the properties of the Plexiglas sidewall and the use of isothermal condition at the outer edge of the domain, which may not represent the experimental conditions accurately enough.

   Close to the sidewall, for $\xi = 0.13$, we see that the addition of the insulation layer and thermal side shields affect the temperature gradient in the simulations. Again the simulations with helium and neon do not capture the trend with *C* that is found in the experiments. We do not yet fully understand the origin of the differences with the experimental observations. The reason is that there are many parameters, such as porosity, the temperature boundary conditions at the outer surface of the insulation and the thermal properties of the materials, which influence the specific results. All these properties are not precisely known from the experiments, which makes it impossible to match experiments and simulations exactly. We also note that the simulations are perfectly azimuthally homogeneous, and the presented simulation data are averaged in the azimuthal direction. The experimental measurements, in contrast, are performed at one azimuthal location, which might not be fully representative of the azimuthal average.
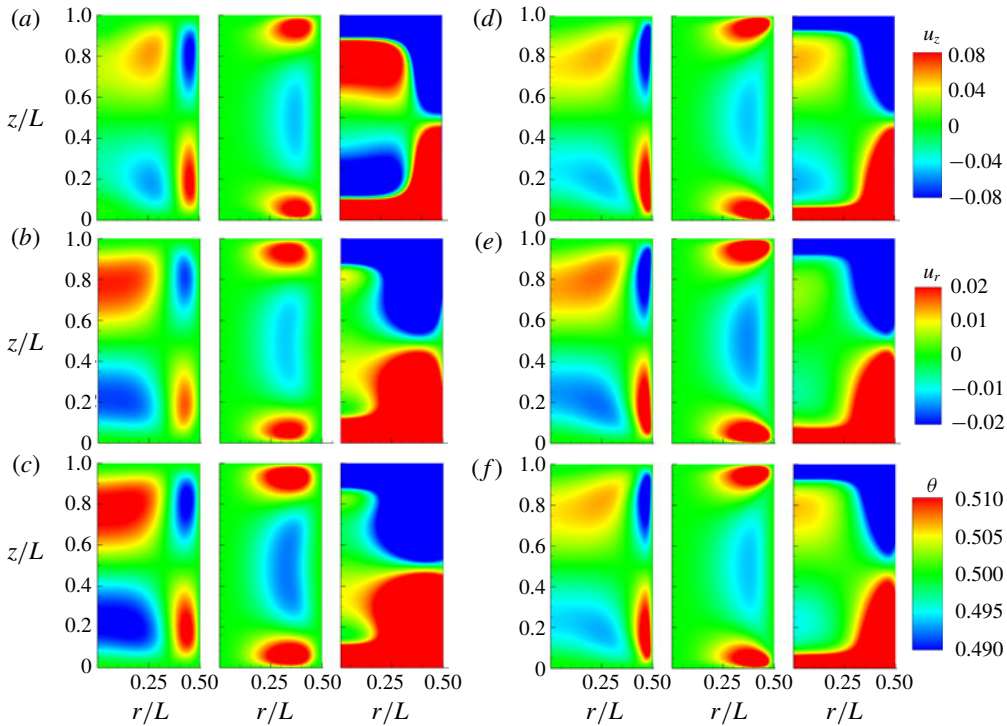
FIGURE 9. (Colour online) The time and azimuthally averaged vertical and radial velocities and temperature for (*a–c*) $Ra = 3 \times 10^5$ and (*d–f*) $Ra = 1 \times 10^7$ with neon as working fluid. (*a,d*) Adiabatic sidewall; (*b,e*) Plexiglas sidewall; (*c,f*) Plexiglas sidewall, additional insulation layer and thermal shields. Left panel: $\langle u_z \rangle_{t,\phi}$, middle panel: $\langle u_r \rangle_{t,\phi}$, right panel: $\langle \theta \rangle_{t,\phi}$.

Finally, in figure 9 we show the azimuthally averaged mean velocity for the three model configurations for $Ra = 3 \times 10^5$ and $Ra = 10^7$. As explained in Kunnen *et al.* (2011), the structure shown in these azimuthally averaged radial and axial velocity maps are a result of a titled LSC as sketched in figure 10. It is immediately clear from figure 9 that the addition of the Plexiglas sidewall results in a noticeable change in the LSC. For the simulations with the adiabatic sidewall the temperature gradient at the cylinder axis is stabilizing. In contrast, when the sidewall is added the adjusted LSC, which is created due to the coupling between the fluid and sidewall dynamics, supports a small destabilizing temperature gradient at the cylinder axis.

6. Summary and conclusions

We performed experiments and DNSs for a $\Gamma = 1.00$ cylindrical Rayleigh–Bénard convection cell, focusing on the effect of the sidewall. We measured the heat transport and the vertical temperature gradient in the horizontal mid-plane both on the cylinder axis and close to the sidewall for $2 \times 10^5 \leqslant Ra \leqslant 4 \times 10^{10}$. We find agreement between *Nu* obtained from experiments and simulations with an adiabatic sidewall for $Ra \lesssim 10^7$ and $Ra \gtrsim 10^9$. For $Ra \gtrsim 10^8$ we also find an agreement for the temperature gradients at the cylinder axis measured in experiments and simulations, even when we use an idealized adiabatic sidewall in the simulations. Both experiments and simulations
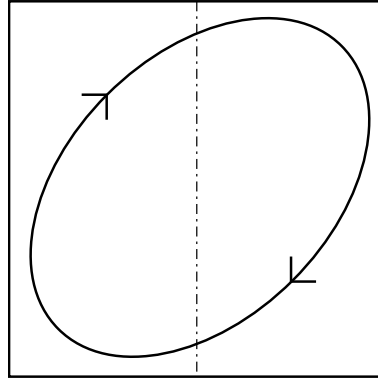
FIGURE 10. Schematic side view of the tilted LSC in the cylinder. The dash-dotted line is the axis of the cylinder.

showed a stabilizing (positive) temperature gradient, see (4.1), at the sample centre, which had not been observed before for $Pr \simeq 0.7$ (Tilgner *et al.* 1993; Brown & Ahlers 2007). Near the sidewall, both simulations and experiments show a small destabilizing temperature gradient for $Ra \gtrsim 10^8$.

However, for $Ra \lesssim 10^8$ significant differences between experiments and simulations with an adiabatic sidewall are observed. In the simulations, the temperature gradient at the cylinder axis remained positive and increased with decreasing Ra, while the experimental values decrease and become negative. A relatively rapid decrease occurred both at the sample centre and near the sidewall. The Ra range over which this decrease occurred depended on the employed gas. The decrease appeared at a higher Ra for a sample with a smaller sidewall admittance C. As Ra decreased past $Ra \simeq 10^6$, the experimental data indicated a sharp transition, presumably from the onset of the turbulent state as reported by Heslot *et al.* (1987). The C-dependence of these features may explain why they were not seen in the DNS since the adiabatic sidewall corresponds to $C \rightarrow \infty$ and the rapid decrease of the gradients occurs at significantly lower Ra. Indeed, simulations show that the internal temperature gradient becomes negative for $Ra \approx 10^4$ and is -1 at the onset as it should be.

Since the magnitude of the measured temperature gradient depends on the specific working fluid, it seems that the influence of the sidewall on the flow structure is crucial to explain local measurements of the vertical temperature gradient. Therefore, we have simulated the effects of a physical sidewall on the heat transfer and flow dynamics. Based on the experimental results, we used the properties of neon and helium as a working fluid in the simulations. We find that for low Ra, the sidewall indeed has pronounced effects, but these tend to decrease with increasing Ra. One of the essential findings is that the thermodynamic coupling between the sidewall and fluid can lead to significant reorganization of the flow. Thus the effect of the sidewall is not necessarily caused by a parasitic heat flux through the sidewall only, but mainly manifests itself due to changed characteristics of the flow. Specifically, it seems that the sidewall stabilizes the large scale flow when compared to the case when just an adiabatic sidewall is considered. As this constitutes an actual change in the heat transfer, experimental measurements cannot be corrected for this.

The pronounced effect of the sidewall configuration on the flow properties is beautifully shown by local measurements of the vertical temperature gradient

discussed above. For low *Ra*, simulations with an adiabatic sidewall do not even capture the destabilizing temperature gradient at the cell centre, while this feature is reproduced when the sidewall is taken into account. In an attempt to mimic the experimental apparatus as closely as possible, also the insulation layer on the dry surface of the sidewall and the thermal shields have been included in the simulations. From these simulations, it becomes clear that it is extremely complicated to capture all interactions between fluid and sidewall, due to which it remains impossible to reproduce all experimental details. The difficulties arise from the challenge of identifying all relevant design parameters as well as the uncertainty of various model parameters in the full three-dimensional DNS. An important finding is that the simulations reveal that the heat exchange between the sidewall and fluid mainly occurs in the region where the plates and sidewall are connection. This heat flux is, in part, driven by the thermal side shields. Interestingly, this heat flux significantly intensifies when convection in the foam starts. This means that in the design of experiments special attention should be spent on reducing heat currents in this region.

An important conclusion is also that small details matter. While the simulations in which the sidewall, insulation and thermal side shields are represented allow us to reproduce various experimental observations quantitatively, they fail to capture other observations. A notable example is that the simulations do not capture the variation of the temperature gradient at the cylinder axis and close to the sidewall with the sidewall admittance *C*. The reason for this must be that a real laboratory set-up is much more involved and subtle than what we can consider in our simulations. It is evident that even our simulations in which we consider the sidewall properties, insulation layer and the thermal side shield with additional idealized boundary conditions do not allow us to reproduce all experimental observations. The reason for this is that tiny details matter, which should be considered as a warning for experimentalists and people performing simulations.

The simulations reveal that the sidewall can act as an extra heat conductor, which absorbs part of the heat from the fluid near the bottom plate and releases it into the fluid near the top plate. This means that the sidewall can act as a short circuit and the relative importance of this heat transfer circuit is more important at lower *Ra*. This concept is the basic assumption in the models by Ahlers (2000) and Roche *et al.* (2001). Both models consider excess heat entering (leaving) the sidewall at the bottom (top) which then goes sideways into (out of) the fluid in the lower (upper) half of the cell. The advantage of the Roche *et al.* (2001) model is that they devised a one-dimensional model for this process in analytic form which makes computations of the size of the effect easier than using the method by Ahlers (2000) who did everything numerically by solving a two-dimensional heat-flow problem. However, the downside of the Roche *et al.* (2001) model is that it contains an unknown parameter which is supposed to be of order one. But changing this parameter from 0.8 to 1.2 for instance has a significant effect on the sidewall correction. Thus a direct comparison of the simulations with the models is very difficult as the models are based on various assumptions, while the situation is considerably more complicated in the simulations as we have an isothermal temperature boundary condition ($T = 0.5$) on the 'dry' side of the Plexiglas sidewall, a three-dimensional temperature distribution in the sidewall and a set of thermal side shields at various locations in the foam, while these aspects are not represented in the models. All these aspects make a comparison to the model very complicated, which goes outside the scope of the present study. As mentioned above an important result of the present simulations is that the coupling of the flow with a physical sidewall influences the actual heat transfer in Rayleigh–Bénard

convection by changing the flow structure and the models by Ahlers (2000) and Roche *et al.* (2001) cannot correct for this effect. Further research is required to determine what designs can minimize these effects.

Acknowledgements

Appendix A. Time discretization

In this appendix we discuss the implementation of the time discretization of the heat equation (3.2), which reads

$$\frac{\mathrm{D}\theta}{\mathrm{D}t} = \frac{1}{\sqrt{PrRa}} \frac{\rho_f C_f^p}{\rho C^p} \boldsymbol{\nabla} \boldsymbol{\cdot} \left(\frac{\lambda}{\lambda_f} \boldsymbol{\nabla}\theta \right) + h. \tag{A 1}$$

Let us assume that a temperature θ_w must be imposed at the ith spatial node using the forcing term h. If we write the time-discrete version of the above equation we have

$$\frac{\theta_i^{n+1} - \theta_i^n}{\Delta t} + (\boldsymbol{u} \boldsymbol{\cdot} \boldsymbol{\nabla}\theta)_i = \frac{1}{\sqrt{PrRa}} \frac{\rho_f C_f^p}{\rho C^p} \boldsymbol{\nabla} \boldsymbol{\cdot} \left(\frac{\lambda}{\lambda_f} \boldsymbol{\nabla}\theta \right)_i + h_i, \tag{A 2}$$

which we can recast as

$$\frac{\theta_i^{n+1} - \theta_i^n}{\Delta t} = RHS_i + h_i, \tag{A 3}$$

with

$$RHS_i = \frac{1}{\sqrt{PrRa}} \frac{\rho_f C_f^p}{\rho C^p} \boldsymbol{\nabla} \boldsymbol{\cdot} \left(\frac{\lambda}{\lambda_f} \boldsymbol{\nabla}\theta \right)_i - (\boldsymbol{u} \boldsymbol{\cdot} \boldsymbol{\nabla}\theta)_i. \tag{A 4}$$

Following what Fadlun *et al.* (2000) did for the velocity $\boldsymbol{u}$, if we want $\theta_i^{n+1} \equiv \theta_w$ we have to plug this equivalence into (A 3) and solve for h_i, which yields

$$h_i = -RHS_i + \frac{\theta_w - \theta_i^n}{\Delta t}, \tag{A 5}$$

which is equivalent to enforcing directly the temperature θ_w at the desired node.

Appendix B. Details of simulations with adiabatic sidewall

As is indicated in tables 3 and 4 we ensured that an adequate resolution in the bulk (Stevens, Verzicco & Lohse 2010) and boundary layers (Shishkina *et al.* 2010) has been used for all simulations. For example, for $Ra = 2 \times 10^{10}$, $Pr = 0.7$ and $\Gamma = 1.00$ we use a grid resolution of $3072 \times 512 \times 1024$ in the azimuthal, radial and axial, direction, respectively. This means that this simulation is considerably better resolved than similar simulations considered before. For example, in Stevens *et al.* (2010) we found that for $Ra = 2 \times 10^{10}$, $Pr = 0.7$ and $\Gamma = 0.5$ reasonably accurate results are obtained on a $512 \times 128 \times 512$ grid. Later, in Stevens, Lohse & Verzicco (2011) we concluded that a grid of $768 \times 192 \times 768$ leads to better converged flow statistics for this case. However, this still implies that a resolution of $1536 \times 384 \times 768$ would already have been sufficient for the simulation at $Ra = 2 \times 10^{10}$, $Pr = 0.7$ and $\Gamma = 1.00$. Similarly, according to the estimates by Shishkina *et al.* (2010) there should be 12 points inside the boundary layers for a simulation at $Ra = 2 \times 10^{10}$. In this

Ra	$N_\theta \times N_r \times N_z$	N_{BL}	Nu_f	Nu_h	Nu_V
2×10^5	$128 \times 48 \times 96$	21	4.73	4.73	4.73
3×10^5	$128 \times 48 \times 96$	19	5.79	5.79	5.79
5×10^5	$128 \times 48 \times 96$	18	6.87	6.87	6.87
7×10^5	$128 \times 48 \times 96$	16	7.66	7.66	7.68
8×10^5	$128 \times 48 \times 96$	16	7.97	7.97	7.98
1×10^6	$128 \times 48 \times 96$	15	8.57	8.57	8.61
2×10^6	$192 \times 64 \times 128$	18	10.55	10.55	10.58
4×10^6	$192 \times 64 \times 128$	16	12.86	12.87	12.92
6×10^6	$192 \times 64 \times 128$	15	14.51	14.51	14.58
8×10^6	$192 \times 64 \times 128$	14	15.79	15.79	15.79
1×10^7	$192 \times 64 \times 128$	13	16.78	16.78	16.74
2×10^7	$256 \times 96 \times 192$	12	20.39	20.37	20.39
4×10^7	$256 \times 96 \times 192$	10	24.67	24.68	24.67
6×10^7	$384 \times 128 \times 256$	14	27.58	27.64	27.57
1×10^8	$384 \times 128 \times 256$	12	31.86	31.77	31.86
2×10^8	$384 \times 128 \times 256$	10	39.03	39.03	39.03
4×10^8	$384 \times 128 \times 256$	23	47.45	47.48	47.35
6×10^8	$1536 \times 256 \times 512$	21	53.73	53.63	53.98
1×10^9	$1536 \times 256 \times 512$	19	62.74	62.74	62.80
2×10^9	$1536 \times 256 \times 512$	16	77.90	77.83	78.26
4×10^9	$1536 \times 256 \times 512$	14	96.99	97.17	97.02
6×10^9	$3072 \times 512 \times 1024$	30	108.86	109.37	108.94
1×10^{10}	$3072 \times 512 \times 1024$	27	126.71	127.40	125.22
2×10^{10}	$3072 \times 512 \times 1024$	23	159.70	159.21	159.95
4×10^{10}	$3072 \times 512 \times 1024$	20	200.00	200.00	200.66

TABLE 3. Simulations for $Pr = 0.7$ and $\Gamma = 1.00$ with an adiabatic sidewall. The columns from left to right indicate the Ra number, the used resolution in the azimuthal, radial and axial directions ($N_\theta \times N_r \times N_z$), the number of grid points in the boundary layers close to the plates and the Nu number over the full (Nu_f) and last half (Nu_h) of the considered simulation interval, and the volume integral of heat flux $Nu_V = 1 + \sqrt{RaPr}\langle u_z T \rangle_{V,t}$ over the whole simulation interval.

study we used 23 in the boundary layer. Therefore, based on the experience from previous studies, in which we tested the required resolution, we are confident that the simulations in this study are very well resolved. The simulations in which the sidewall and foam layers are added follow the same strict resolution criteria.

Appendix C. Data simulations with physical sidewall

Case	$N_\theta \times N_r \times N_z$	$\dfrac{\rho_s C_s^p}{\rho_f C_f^p}$	$\dfrac{\lambda_s}{\lambda_f}$	$\dfrac{\rho_i C_i^p}{\rho_f C_f^p}$	$\dfrac{\lambda_i}{\lambda_f}$
Neon with Plexiglas sidewall, see table 5	$192 \times 96 \times 128$	1861.2	4.184	—	—
Neon with Plexiglas sidewall, insulation and thermal side shields, see table 6	$192 \times 128 \times 128$	1861.2	4.184	60	0.793
Helium with Plexiglas sidewall, insulation and thermal side shields, see table 7	$192 \times 128 \times 128$	2030.7	1.24	65.5	0.264

TABLE 4. Summary of the simulations using neon and helium as working fluid for $2 \times 10^5 \leqslant Ra \leqslant 10^7$. We performed simulations with just the Plexiglas sidewall and using the Plexiglas sidewall with the additional insulation layer and thermal shields as indicated in figure 1. For $Ra = 10^7$ there are 16 grid points in the Plexiglas sidewall and 48 grid points in the insulation layer; ρ, C^p and λ are, respectively, the density, constant pressure specific heat and thermal conductivity. The subscripts f, s and i refer to the fluid, sidewall and insulation, respectively. The Nu data are given in tables 5–7 as indicated.

Ra	Nu
2.0×10^5	5.57 ± 0.01
3.0×10^5	6.12 ± 0.01
4.0×10^5	6.53 ± 0.02
5.0×10^5	7.23 ± 0.01
8.0×10^5	7.86 ± 0.01
9.0×10^5	8.15 ± 0.01
1.0×10^6	8.37 ± 0.02
1.3×10^6	9.05 ± 0.02
1.5×10^6	9.40 ± 0.02
1.8×10^6	9.87 ± 0.01
2.0×10^6	10.15 ± 0.02
3.0×10^6	11.39 ± 0.02
4.0×10^6	12.37 ± 0.02
6.0×10^6	13.85 ± 0.03
8.0×10^6	15.06 ± 0.02
1.0×10^7	16.06 ± 0.04

TABLE 5. The Nu number data for the simulations with neon and a Plexiglas sidewall, see table 4.

Ra	Nu
2.0×10^5	5.04 ± 0.01
3.0×10^5	5.68 ± 0.01
4.0×10^5	6.13 ± 0.01
5.0×10^5	6.55 ± 0.01
6.0×10^5	6.91 ± 0.02
8.0×10^5	7.60 ± 0.01
1.0×10^6	8.13 ± 0.01
1.5×10^6	9.26 ± 0.01
2.0×10^6	10.06 ± 0.02
3.0×10^6	11.36 ± 0.02
4.0×10^6	12.32 ± 0.01
5.0×10^6	13.15 ± 0.01
6.0×10^6	13.84 ± 0.02
8.0×10^6	15.02 ± 0.03
1.0×10^7	16.11 ± 0.03

TABLE 6. The *Nu* number data for the simulations with neon and a Plexiglas sidewall with additional insulation layer and thermal side shields, see table 4.

Ra	Nu
2×10^5	5.23 ± 0.01
3×10^5	5.65 ± 0.02
4×10^5	6.21 ± 0.02
5×10^5	6.70 ± 0.01
7×10^5	7.38 ± 0.02
8×10^5	7.78 ± 0.03
9×10^5	8.02 ± 0.02
1×10^6	8.30 ± 0.05
3×10^6	11.42 ± 0.03
5×10^6	13.21 ± 0.05
1×10^7	16.10 ± 0.07

TABLE 7. The *Nu* number data for the simulations with helium and a Plexiglas sidewall with additional insulation layer and thermal side shields, see table 4.

REFERENCES

AHLERS, G. 2000 Effect of sidewall conductance on heat-transport measurements for turbulent Rayleigh–Bénard convection. *Phys. Rev.* E **63** (1), 015303.

AHLERS, G. 2009 Turbulent convection. *Physics* **2**, 74.

AHLERS, G., BODENSCHATZ, E. & HE, X. 2014 Logarithmic temperature profiles of turbulent Rayleigh–Bénard convection in the classical and ultimate state for a Prandtl number of 0.8. *J. Fluid Mech.* **758**, 436–467.

AHLERS, G., GROSSMANN, S. & LOHSE, D. 2009 Heat transfer and large scale dynamics in turbulent Rayleigh–Bénard convection. *Rev. Mod. Phys.* **81** (2), 503–537.

ASHKENAZI, S. & STEINBERG, V. 1999 High Rayleigh number turbulent convection in a gas near the gas–liquid critical point. *Phys. Rev. Lett.* **83**, 3641–3644.

BODENSCHATZ, E., PESCH, W. & AHLERS, G. 2000 Recent developments in Rayleigh–Bénard convection. *Annu. Rev. Fluid Mech.* **32** (1), 709–778.

BREUER, M., WESSLING, S., SCHMALZL, J. & HANSEN, U. 2004 Effect of inertia in Rayleigh–Bénard convection. *Phys. Rev.* E **69**, 026302.

BROWN, E. & AHLERS, G. 2006 Effect of the Earth's Coriolis force on turbulent Rayleigh–Bénard convection in the laboratory. *Phys. Fluids* **18**, 125108.

BROWN, E. & AHLERS, G. 2007 Temperature gradients, and search for non-Boussinesq effects, in the interior of turbulent Rayleigh–Bénard convection. *Eur. Phys. Lett.* **80** (1), 14001.

BROWN, E. & AHLERS, G. 2008a Azimuthal asymmetries of the large-scale circulation in turbulent Rayleigh–Bénard convection. *Phys. Fluids* **20**, 105105.

BROWN, E. & AHLERS, G. 2008b A model of diffusion in a potential well for the dynamics of the large-scale circulation in turbulent Rayleigh–Bénard convection. *Phys. Fluids* **20**, 075101.

BROWN, E., NIKOLAENKO, A. & AHLERS, G. 2005 Reorientation of the large-scale circulation in turbulent Rayleigh–Bénard convection. *Phys. Rev. Lett.* **95**, 084503.

BUELL, J. C. & CATTON, I. 1983 The effect of wall conduction on the stability of a fluid in a right circular–cylinder heated from below. *Trans. ASME J. Heat Transfer* **105**, 255–260.

CHAVANNE, X., CHILLÀ, F., CHABAUD, B., CASTAING, B., CHAUSSY, J. & HÉBRAL, B. 1996 High Rayleigh number convection with gaseous Helium at low temperature. *J. Low Temp. Phys.* **104**, 109–129.

CHILLÀ, F. & SCHUMACHER, J. 2012 New perspectives in turbulent Rayleigh–Bénard convection. *Eur. Phys. J.* E **35** (7), 1–25.

FADLUN, E. A., VERZICCO, R., ORLANDI, P. & MOHD-YUSOF, J. 2000 Combined immersed-boundary finite-difference methods for three-dimensional complex flow simulations. *J. Comput. Phys.* **161** (1), 35–60.

GROSSMANN, S. & LOHSE, D. 2000 Scaling in thermal convection: a unifying theory. *J. Fluid Mech.* **407**, 27–56.

GROSSMANN, S. & LOHSE, D. 2001 Thermal convection for large Prandtl numbers. *Phys. Rev. Lett.* **86** (15), 3316–3319.

HE, X., VAN GILS, D. P. M., BODENSCHATZ, E. & AHLERS, G. 2015 Reynolds numbers and the elliptic approximation near the ultimate state of turbulent Rayleigh–Bénard convection. *New J. Phys.* **17**, 063028.

HÉBERT, F., HUFSCHMID, R., SCHEEL, J. & AHLERS, G. 2010 Onset of Rayleigh–Bénard convection in cylindrical containers. *Phys. Rev.* E **81**, 046318.

HESLOT, F., CASTAING, B. & LIBCHABER, A. 1987 Transition to turbulence in helium gas. *Phys. Rev.* A **36**, 5870–5873.

KRISHNAMURTI, R. 1970 On the transition to turbulent convection. Part 2. The transition to time-dependent flow. *J. Fluid Mech.* **42**, 309–320.

KUNNEN, R. P. J., STEVENS, R. J. A. M., OVERKAMP, J., SUN, C., VAN HEIJST, G. J. F. & CLERCX, H. J. H. 2011 The role of Stewartson and Ekman layers in turbulent rotating Rayleigh–Bénard convection. *J. Fluid Mech.* **688**, 422–442.

LANDAU, L. D. & LIFSHITZ, E. M. 1987 *Fluid Mechanics*. Pergamon Press.

LOHSE, D. & XIA, K.-Q. 2010 Small-scale properties of turbulent Rayleigh–Bénard convection. *Annu. Rev. Fluid Mech.* **42**, 335–364.

MUELLER, K. H., AHLERS, G. & POBELL, F. 1976 Thermal expansion coefficient, scaling, and universality near the superfluid transition of ^{4}He under pressure. *Phys. Rev.* B **14**, 2096–2117.

NIEMELA, J. J., SKRBEK, L., SREENIVASAN, K. R. & DONNELLY, R. J. 2000 Turbulent convection at very high Rayleigh numbers. *Nature* **404** (6780), 837–840.

NIEMELA, J. J. & SREENIVASAN, K. R. 2003 Confined turbulent convection. *J. Fluid Mech.* **481**, 355–384.

ROCHE, P.-E., CASTAING, B., CHABAUD, B., HÉBRAL, B. & SOMMERIA, J. 2001 Sidewall effects in Rayleigh–Bénard experiments. *Eur. Phys. J.* B **24** (3), 405–408.

SCHEEL, J. D., KIM, E. & WHITE, K. R. 2012 Thermal and viscous boundary layers in turbulent Rayleigh–Bénard convection. *J. Fluid Mech.* **711**, 281–305.

SCHMALZL, J., BREUER, M. & HANSEN, U. 2002 The influence of the Prandtl number on the style of vigorous thermal convection. *Geophys. Astrophys. Fluid Dyn.* **96**, 381–403.

SHISHKINA, O., STEVENS, R. J. A. M., GROSSMANN, S. & LOHSE, D. 2010 Boundary layer structure in turbulent thermal convection and its consequences for the required numerical resolution. *New J. Phys.* **12**, 075022.

SHISHKINA, O. & THESS, A. 2009 Mean temperature profiles in turbulent Rayleigh–Bénard convection of water. *J. Fluid Mech.* **633**, 449–460.

STEVENS, R. J. A. M., LOHSE, D. & VERZICCO, R. 2011 Prandtl and Rayleigh number dependence of heat transport in high Rayleigh number thermal convection. *J. Fluid Mech.* **688**, 31–43.

STEVENS, R. J. A. M., LOHSE, D. & VERZICCO, R. 2014 Sidewall effects in Rayleigh–Bénard convection. *J. Fluid Mech.* **741**, 1–27.

STEVENS, R. J. A. M., VAN DER POEL, E. P., GROSSMANN, S. & LOHSE, D. 2013 The unifying theory of scaling in thermal convection: the updated prefactors. *J. Fluid Mech.* **730**, 295–308.

STEVENS, R. J. A. M., VERZICCO, R. & LOHSE, D. 2010 Radial boundary layer structure and Nusselt number in Rayleigh–Bénard convection. *J. Fluid Mech.* **643**, 495–507.

TILGNER, A., BELMONTE, A. & LIBCHABER, A. 1993 Temperature and velocity profiles of turbulent convection in water. *Phys. Rev.* E **47** (4), R2253–R2256.

VERZICCO, R. 2002 Sidewall finite-conductivity effects in confined turbulent thermal convection. *J. Fluid Mech.* **473**, 201–210.

WEI, P. & AHLERS, G. 2014 Logarithmic temperature profiles in the bulk of turbulent Rayleigh–Bénard convection for a Prandtl number of 12.3. *J. Fluid Mech.* **758**, 809–830.

XIA, K.-Q. 2013 Current trends and future directions in turbulent thermal convection. *Theor. Appl. Mech. Lett.* **3** (5), 052001.

ZHONG, J.-Q. & AHLERS, G. 2010 Heat transport and the large-scale circulation in rotating turbulent Rayleigh–Bénard convection. *J. Fluid Mech.* **665**, 300–333.